

Analysis of Sensing in OFDM-based ISAC under the Influence of Sampling Jitter

Lucas Giroto, *Member, IEEE*, Andrei Camponogara, Yueheng Li *Member, IEEE*,
Jiayi Chen, *Graduate Student Member, IEEE*, Lukas Sigg, Thomas Zwick, *Fellow, IEEE*,
and Benjamin Nuss, *Senior Member, IEEE*

Abstract—To enable integrated sensing and communication (ISAC) in cellular networks, a wide range of additional requirements and challenges are either imposed or become more critical. One such impairment is sampling jitter (SJ), which arises due to imperfections in the sampling instants of the clocks of digital-to-analog converters (DACs) and analog-to-digital converters (ADCs). While SJ is already well studied for communication systems based on orthogonal frequency-division multiplexing (OFDM), which is expected to be the waveform of choice for most sixth-generation (6G) scenarios where ISAC could be possible, the implications of SJ on the OFDM-based radar sensing must still be thoroughly analyzed. Considering that phase-locked loop (PLL)-based oscillators are used to derive sampling clocks, which leads to colored SJ, i.e., SJ with non-flat power spectral density, this article analyzes the resulting distortion of the adopted digital constellation modulation and sensing performance in OFDM-based ISAC for both baseband (BB) and bandpass (BP) sampling strategies and different oversampling factors. For BB sampling, it is seen that SJ induces intercarrier interference (ICI), while for BP sampling, it causes carrier phase error and more severe ICI due to a phase noise-like effect at the digital intermediate frequency. Obtained results for a single-input single-output OFDM-based ISAC system with various OFDM signal parameterizations demonstrate that SJ-induced degradation becomes non-negligible for both BB and BP sampling only for root mean square (RMS) SJ values above 10^{-11} s at both DAC and ADC, which corresponds to 0.5×10^{-2} times the considered critical sampling period without oversampling.

Based on the achieved results, it can be concluded that state-of-the-art hardware enables sufficient communication and sensing robustness against SJ, as RMS SJ values in the femtosecond range can be achieved.

Index Terms—6G, integrated sensing and communication (ISAC), orthogonal frequency-division multiplexing (OFDM), oscillator phase noise (PN), sampling jitter (SJ).

I. INTRODUCTION

WITH the advent of sixth generation (6G) networks [1], integrated sensing and communication (ISAC) is expected to emerge as a pivotal technology [2]–[5]. The principle of ISAC consists of simultaneously performing communication and radar sensing with shared hardware and spectral resources [6], [7]. With the added sensing functionality to the cellular infrastructure, a wide range of novel applications is expected to become possible. These include, e.g., environment sensing in urban scenarios to enable safe mobility and automation in intralogistics scenarios involving humans and automatic guided vehicles (AGVs) [8]–[10]. As a result, ISAC is set to play a transformative role in next-generation cellular networks, with early developments anticipated in upcoming 3rd Generation Partnership Project (3GPP) 6G releases.

One of the key challenges in ISAC is enabling accurate radar sensing while meeting the main demand of 6G cellular networks, which is to support robust connectivity at high data rates [11], [12]. This is facilitated by the use of the multicarrier modulation scheme orthogonal frequency-division multiplexing (OFDM) [13], which is already employed in current fifth generation (5G) cellular systems and will most likely also be the choice for 6G. Besides a proper allocation of radio resources between communication and radar sensing, this requires jointly tackling impairments associated with one or both applications [14], [15]. Among these are high isolation between closely located transmit and receive antenna arrays and self-interference cancellation (SIC) requirements due to the required in-band full duplex (IBFD) operation for some communication applications and monostatic radar sensing [16]–[18], or hardware non-idealities which may lead to synchronization issues or signal impairments for communication and bistatic radar sensing [19], [20]. Among aforementioned non-idealities are time and frequency offset [21], [22], sampling frequency offset (SFO) [23], [24], oscillator phase noise (PN) [25], [26], and sampling jitter (SJ) [27], [28], whose implications have already been widely studied for OFDM-based communication systems. In the OFDM-based

The authors acknowledge the financial support by the Federal Ministry of Education and Research of Germany in the projects “KOMSENS-6G” (grant number: 16KISK123) and “Open6GHub” (grant number: 16KISK010). (*Corresponding author: Lucas Giroto.*)

L. Giroto was with the Institute of Radio Frequency Engineering and Electronics (IHE), Karlsruhe Institute of Technology (KIT), 76131 Karlsruhe, Germany. He is now with Nokia Bell Labs, 70469 Stuttgart, Germany (e-mail: lucas.giroto@nokia-bell-labs.com).

Á Camponogara is with the Electrical Engineering Department, Federal University of Paraná, Curitiba, PR 81530-000, Brazil (e-mail: andrei.camponogara@ufpr.br).

Y. Li was with the Institute of Radio Frequency Engineering and Electronics (IHE), Karlsruhe Institute of Technology (KIT), 76131 Karlsruhe, Germany. He is now with the Institute of Intelligent Communication Technology, Shandong University (SDU), 250100 Jinan, China (e-mail: yueheng.li@sdu.edu.cn).

J. Chen and T. Zwick are with the Institute of Radio Frequency Engineering and Electronics (IHE), Karlsruhe Institute of Technology (KIT), 76131 Karlsruhe, Germany (e-mail: jiayi.chen@kit.edu, thomas.zwick@kit.edu).

L. Sigg was with the Institute of Radio Frequency Engineering and Electronics (IHE), Karlsruhe Institute of Technology (KIT), 76131 Karlsruhe, Germany. He is now with MBDA Germany, 86529 Schrobenhausen, Germany (e-mail: lukas.sigg@mbda-systems.de).

B. Nuss was with the Institute of Radio Frequency Engineering and Electronics (IHE), Karlsruhe Institute of Technology (KIT), 76131 Karlsruhe, Germany. He is now with the Professorship of Microwave Sensors and Sensor Systems, Technical University of Munich, 80333 Munich, Germany. (e-mail: benjamin.nuss@tum.de).

radar and ISAC context, recent studies have investigated the influence of most of these issues on radar sensing performance and proposed compensation strategies where feasible [29]–[36]. However, the effects of SJ on OFDM-based sensing performance have been overlooked.

SJ refers to the deviation in digital-to-analog converter (DAC) or analog-to-digital converter (ADC) sampling instants caused by imperfections in clock timing [20]. According to [37], SJ is composed of both aperture jitter, which represents the sampling time variations caused by noise in the sample-and-hold circuit of an ADC, and clock jitter, which is raised by the clock generator used to feed the ADC with a clock signal. The analysis in this study shows that, for short signal block durations as is typically the case in millimeter wave (mmWave) OFDM-based communication, clock jitter is the dominant effect. In addition, it is shown that increasing oversampling is ineffective against clock jitter-induced interference. Unlike aperture jitter that is spread over the whole digitization band, this happens since clock jitter interference is concentrated within the frequency band occupied by the input signal to an ADC. Out of this reason, numerous studies consider only the effect of clock jitter.

When experienced in OFDM-based systems with baseband (BB) sampling, SJ leads to intercarrier interference (ICI) [20]. For the case where bandpass (BP) sampling is adopted, [38] and [28] presented an analysis of ADC SJ on an OFDM-based communication system. These studies showed that, besides ICI, SJ results in an oscillator PN-like effect due to the use of a digital intermediate frequency (IF), leading to common phase error (CPE). For the BB sampling case, [27], [39] investigated the effect of oversampling on the ICI induced by white ADC SJ, where the SJ at different sampling time instants is uncorrelated as opposed to colored SJ which has non-flat power spectral density (PSD), without considering DAC SJ. Furthermore, [40] derived closed-form expressions and upper bounds for the ICI power due to white and colored ADC SJ only, also considering the effect of oversampling. It was shown that, for colored SJ, oversampling is not as effective as for the white SJ case, and that a residual ICI is always present.

Shifting the focus from the receiver to the transmitter side, [41] presented an analysis of white DAC SJ, showing that it leads to out-of-band (OOB) radiation and investigating spectral sidelobe suppression techniques to compensate for it. Finally, [42], analyzed the effects of white and colored SJ at both ADC and DAC for hybrid OFDM-digital filter multiple access passive optical networks. Afterwards, the authors proposed a SJ simulation model consisting of oversampling, a fractional delay filter at the increased sampling rate, and downsampling. Based on the obtained results, it was concluded that the effects of SJ are virtually the same regardless of whether they take place at a DAC or an ADC. In addition, it was observed that oversampling at the ADC is ineffective against DAC jitter.

In future 6G ISAC systems, which are expected to operate at increasingly higher frequencies and require tighter synchronization margins, understanding the effects of SJ and its implications on not only communication, but also on the radar sensing performance becomes crucial. In addition, to better understand how sampling jitter can affect the performance of

OFDM-based ISAC, a larger variety of OFDM signal parameters (i.e., number of subcarriers and modulation alphabet) than in the aforementioned studies needs to be considered. Furthermore, a SJ model that better reflects the behavior of state-of-the-art hardware must be adopted. Such model should, e.g., consider the use of phase-locked loop (PLL)-based oscillators to derive DAC and ADC sampling clocks, which leads to colored SJ.

In this sense, this article investigates the impact of colored SJ raised by the use of a PLL-based oscillator to generate the sampling clock of single-input single-output (SISO) OFDM-based ISAC systems. In this context, both communication and radar sensing impairment are assessed. Specifically, the degradation of the constellation shapes induced by SJ at both DAC and ADC is analyzed using error vector magnitude (EVM) and signal-to-interference ratio (SIR) as parameters. In addition, both BB and BP sampling strategies, as well as several distinct numbers of OFDM subcarriers, modulation orders, and oversampling factors used in frequency-domain zero padding (FDZP) are considered. Next, the resulting implications on the radar sensing capabilities of OFDM-based ISAC systems are analyzed. For that purpose, the degradation of main and sidelobes of radar target reflections, as well as the SIR reduction due to SJ is analyzed for the aforementioned sets of parameters.

The contributions of this article can be summarized as follows:

- A mathematical formulation of the effects of SJ is presented. A closed-form expression is provided that relates the received OFDM symbols in the discrete-frequency domain to both the transmitted OFDM symbols and the SJ at the DAC and ADC stages.
- A numerical analysis is conducted on the impact of colored SJ, caused by PN in PLL-based oscillators, on OFDM-based ISAC systems with various waveform configurations. These include different constellation sizes, oversampling factors for FDZP at the transmitter side, and subcarrier numbers. EVM and SIR are used to quantify constellation distortions, while radar sensing is assessed using peak power loss ratio (PPLR), peak sidelobe level ratio (PSLR) and integrated sidelobe level ratio (ISLR) in both range and Doppler shift directions of radar images, and the SIR of target reflections in radar images, henceforth referred to as image SIR.
- A comparison of OFDM-based ISAC systems with BB and BP sampling strategies under the influence of SJ is presented. While it is known in the literature that SJ leads to ICI when BB sampling is adopted as well as in both ICI and CPE in the BP sampling case as SJ results in a PN-like effect at the digital IF, the consequences of these effects on the sensing is quantified and analyzed in this article.

The remainder of this article is organized as follows. Section II formulates the system model of an OFDM-based ISAC system impaired SJ. Sections III and IV present analyses of the SJ-induced impairment of the considered ISAC system under SJ influence for communication and radar sensing,

respectively. To conclude the discussion, Section V provides final remarks and discusses the implications of the findings of this article.

II. SYSTEM MODEL

At the transmitter side of the considered SISO OFDM-based ISAC system, constellation symbols $\mathbf{d}_{\text{Tx}}^{\text{OFDM}} \in \mathbb{C}^{N \times 1}$ are mapped into a discrete-frequency domain transmit OFDM symbol $\mathbf{S} \in \mathbb{C}^{N \times 1}$ that contains $N \in \mathbb{N}_{>0}$ subcarriers spaced by $\Delta f = B/N$, where B is the BB bandwidth later occupied by the OFDM signal. It is worth emphasizing that, although the following formulation assumes a single OFDM symbol for clarity and without loss of generality, a frame containing multiple OFDM symbols is typically transmitted in practice. The transmitter processing chain continues with FDZP, which consists of appending empty subcarriers to the edges of the OFDM symbol in the discrete-frequency domain, to perform oversampling with factor $\eta \in \mathbb{N}_{>0}$, which results in the OFDM symbol $\mathbf{X} \in \mathbb{C}^{\eta N \times 1}$. Next, by inverse discrete Fourier transform (IDFT) is performed on \mathbf{X} and cyclic prefix (CP) prepending to the resulting discrete-time domain OFDM symbol. The resulting discrete-time domain transmit OFDM symbol is denoted as $\mathbf{x}_{\text{CP}} \in \mathbb{C}^{\eta(N+N_{\text{CP}}) \times 1}$, where N_{CP} is the CP length without oversampling. \mathbf{x}_{CP} then undergoes parallel-to-serial (P/S) conversion to form a stream of samples that finally undergoes digital-to-analog (D/A) conversion with sampling rate $F_s^\eta = \eta B$. Consequently, a sampling period $T_s^\eta = 1/F_s^\eta = 1/(\eta B)$, which is η times smaller than the critical sampling period $T_s = 1/B$, is obtained. The resulting BB analog signal $x_{\text{BB}}(t) \in \mathbb{C}$ from D/A conversion with an ideal, bandlimited DAC to $f \in [-F_s/2, F_s/2]$, where f denotes frequency, can be expressed as

$$x_{\text{BB}}(t) = \sum_{\nu=-\eta N_{\text{CP}}}^{\eta N-1} x_\nu \frac{\sin(\pi(t - \nu T_s/\eta)/(T_s/\eta))}{\pi(t - \nu T_s/\eta)/(T_s/\eta)} \quad (1)$$

for $-T_{\text{CP}} \leq t < T$, where $T_{\text{CP}} = N_{\text{CP}} T_s$ and $T = N T_s$ are the durations of the CP and the OFDM symbol disregarding CP, respectively. In (1), $x_\nu \in \mathbb{C}$ is the ν th sample, $\nu \in \{-\eta N_{\text{CP}}, -\eta N_{\text{CP}} + 1, \dots, \eta N - 1\}$, of \mathbf{x}_{CP} .

The expression in (1) is only valid for ideal sampling instants. In practice, however, the DAC sampling clock is usually derived from a PLL-based oscillator, which has a PN $\theta_{\text{DAC}}^{\text{PN}}(t) \in \mathbb{R}$ with double-sided PSD $S_{\theta_{\text{DAC}}^{\text{PN}}}(f) \in \mathbb{R}_{\geq 0}$ [20], [43]–[45]. The presence of the PN $\theta_{\text{DAC}}^{\text{PN}}(t)$ in the oscillator used to derive the sampling clock ultimately leads to a SJ $\delta_{\text{SJ}}^{\text{DAC}}(t) \in \mathbb{R}$, whose relationship to the aforementioned PN can be expressed as [20]

$$\delta_{\text{SJ}}^{\text{DAC}}(t) = \theta_{\text{DAC}}^{\text{PN}}(t)/(2\pi F_s^\eta). \quad (2)$$

Considering the effect of SJ and neglecting further impairments such as SFO, $x_{\text{BB}}(t) \in \mathbb{C}$ becomes $x_{\text{BB}}^{\text{SJ}}(t) \in \mathbb{C}$, and (1) can be rewritten as (3).

Assuming a noiseless, ideal single-path channel and still neglecting further impairments, the receive BB signal $y_{\text{BB}}(t) \in \mathbb{C}$ can simply be expressed as

$$y_{\text{BB}}(t) = x_{\text{BB}}^{\text{SJ}}(t). \quad (4)$$

After sampling at an ADC with SJ $\delta_{\text{SJ}}^{\text{ADC}}(t) \in \mathbb{R}$ also resulting from the use of a PLL-based oscillator to derive the sampling clock, the ν' th sample $y_{\nu'} \in \mathbb{C}$, $\nu' \in \{-\eta N_{\text{CP}}, -N_{\text{CP}} + 1, \dots, \eta N - 1\}$, of the discrete-time domain receive OFDM symbol $\mathbf{y}_{\text{CP}} \in \mathbb{C}^{\eta(N+N_{\text{CP}}) \times 1}$ is obtained as

$$\begin{aligned} y_{\nu'} &= y_{\text{BB}}(\nu' T_s/\eta + \delta_{\text{ADC}}^{\text{SJ}}(\nu' T_s/\eta)) \\ &= x_{\text{BB}}^{\text{SJ}}(\nu' T_s/\eta + \delta_{\text{ADC}}^{\text{SJ}}(\nu' T_s/\eta)) \end{aligned} \quad (5)$$

To expand (5), (4) and (3) are used, which results in (6). Next, the CP is removed from \mathbf{y}_{CP} , and a discrete Fourier transform (DFT) is performed to produce the discrete-frequency domain receive OFDM symbol $\mathbf{Y} \in \mathbb{C}^{N \times 1}$, whose l th element, $l \in \{-\eta N/2, -\eta N/2 + 1, \dots, \eta N/2 - 1\}$, is expressed as

$$Y_l = \sum_{\nu'=0}^{\eta N-1} y_{\nu'} \exp^{j2\pi \frac{l\nu'}{\eta N}}. \quad (7)$$

The expression in (6) is then substituted into (7) to yield (8).

Assuming $\omega = \pi/(T_s/\eta)$, the fraction in (8) can be rewritten as the function $\varphi(\nu, \nu')$ of ν and ν' in (9). Expanding (9) via Taylor series and keeping only the first two terms yields (10). The latter equation can be further rewritten as (11), which allows rewriting (8) as (12). After discarding the subcarriers added at the transmitter side for FDZP, the discrete-frequency domain receive OFDM symbol $\mathbf{R} \in \mathbb{C}^{N \times 1}$ is obtained. Since $(\eta - 1)N$ inactive subcarriers are added at the transmitter side for FDZP, $(\eta - 1)N/2$ to the left and $(\eta - 1)N/2$ to the right of the discrete-frequency domain spectrum, the k th element $R_k \in \mathbb{C}$, $k \in \{-N/2, -N/2 + 1, \dots, N/2 - 1\}$, of \mathbf{R} is expressed as

$$R_k = Y_{k+\eta N/2+1}. \quad (13)$$

An analysis of the obtained expressions in (12) and (13) reveals that the non-ideal sampling results in an ICI term that depends on all discrete-time domain samples, including the ones in the CP, as well as their mutual leakage due to SJ at both DAC and ADC. If only SJ at the DAC is considered, it is known that unwanted OOB radiation will occur [41]. Combined with ADC SJ, this will not only result in ICI among the subcarriers of interest, but in more severe ICI due to the leakage into the subcarriers originally used for FDZP at the transmitter side that were supposed to be inactive. The aforementioned issues are the only impairments induced by SJ when BB sampling is performed. When BP sampling is adopted instead, the transmit samples undergo digital up-conversion (DUC) to an IF before D/A conversion at the transmitter side, and the receive samples undergo digital down-conversion (DDC) from the IF into the baseband after analog-to-digital (A/D) conversion at the receiver side. Consequently, not only OOB radiation due to DAC SJ and ICI due to both DAC and ADC SJ occur, but also a PN-like effect is induced to the IF as discussed in [38], which in turn results in more ICI and CPE [36]. The implications of the discussed degradations induced by SJ and their effects on the communication and radar sensing in OFDM-based ISAC systems with both BB and BP sampling are analyzed in Sections III and IV, respectively.

TABLE I
ADOPTED OFDM SIGNAL PARAMETERS

Carrier frequency (f_c)	26.2 GHz
Bandwidth (B)	500 MHz
Critical sampling period (T_s)	2 ns
Digital IF (f_{IF})	{0 Hz, 1 GHz}
Oversampling factor (η)	{1, 2, 4, 8}
No. of subcarriers (N)	{256, 512, 1024, 2048, 4096, 8192, 16384}
CP length (N_{CP})	{0, $N/4$, N }
No. of OFDM symbols (M)	{128}
Modulation alphabet	{QPSK, 16-QAM, 64-QAM, 256-QAM}

III. NUMERICAL RESULTS FOR COMMUNICATION

To analyze the SJ-induced impairments in an mmWave OFDM-based ISAC system, the set of OFDM signal parameters listed in Table I are adopted, being the specifically considered parameter values are mentioned in the following subsections. The digital IFs $f_{IF} = 0$ Hz and $f_{IF} = 1$ GHz are for BB and BP sampling, respectively. As for the adopted radio-frequency (RF) carrier and frequency bandwidth in Table I, they are close to what is typically adopted at initial part of the 5G New Radio (5G NR) Frequency Range 2 (FR2). The somewhat deviating values from the 5G NR were chosen to yield reasonable performance due to the constraints in the measurement setup for ISAC measurements adopted in previous works [35], [36], [46].

Besides the aforementioned OFDM signal parameters, the PLL-based oscillator PN model from [20] is adopted. Its parameters were chosen to match the PN PSD reported for the PLL contained in the Texas Instruments LMX2594 RF synthesizer [47] for the closest frequency to the 122.88 MHz reference oscillator. Both the aforementioned PLL and sampling clock frequency are used for the reference oscillator from which the sampling clocks of DAC and ADC tiles are generated in the Zynq UltraScale+ RFSoc ZCU111 system-on-a-chip (SoC) platform [48]. In reality, however, the oscillator signal passes through a Texas Instruments LMK04208 low-noise clock jitter cleaner with dual loop PLLs [49], which shapes the PN PSD and eventually reduces the resulting SJ.

For simplicity, the jitter cleaner LMK04208 is disregarded from the following analyses, the root mean square (RMS) SJ associated with the LMX2594 is varied instead to allow analyzing the effect of a wider range of SJ RMS values on the communication and radar sensing performance in the considered OFDM-based ISAC system. The adopted PN model, which was based on data from the LMX2594 data sheet [47], has the double-sided PN PSD shown in Fig. 1a and the integrated PN level shown in Fig. 1b. A PN time series was then generated based on the aforementioned PSD, and the resulting SJ from the aforementioned PLL-based oscillator PN calculated according to (2). The resulting SJ probability density function (PDF) is shown in Fig. 1d. Due to the fact that the considered PN PSD from Fig. 1a is not flat, the SJ will be colored. Moreover, since individual RF synthesizers and therefore PLLs are used for the DAC and ADC tiles in the Zynq UltraScale+ RFSoc ZCU111, the DAC and ADC SJs $\delta_{SJ}^{DAC}(t)$ and $\delta_{SJ}^{ADC}(t)$ are henceforth assumed to be uncorrelated regardless of whether a monostatic or bistatic ISAC architecture is assumed and communication or sensing is performed.

Next, the SJ-induced communication performance degradation in an OFDM-based ISAC system over an ideal, noiseless channel as assumed in Section II is analyzed. For that, EVM and SIR are adopted as performance parameters. Results and discussions are presented for both BB and BP sampling strategies in Sections III-A and III-B, respectively, and remarks on the presented simulation results are given in Section III-C.

A. Baseband Sampling

In Fig. 2, the achieved mean EVM is shown as a function of the number of subcarriers N for all digital modulation schemes from Table I, namely QPSK, 16-QAM, 64-QAM and 256-QAM. In addition, the case where no FDZP was performed, i.e., $\eta = 1$, as well as the cases with FDZP oversampling factors of $\eta \in \{2, 4, 8\}$ were analyzed. The achieved results assume the use of the SJ model with PDF depicted in Fig. 1d, which was derived from the PN PSD in Fig. 1a, but with varying RMS values to better analyze the effects of different SJ levels. The adopted SJ RMS values,

$$x_{BB}^{SJ}(t) = \sum_{\nu=-\eta N_{cp}}^{\eta N-1} x_{\nu} \frac{\sin(\pi [t - (\nu T_s/\eta + \delta_{DAC}^{SJ}(\nu T_s/\eta))] / (T_s/\eta))}{\pi [t - (\nu T_s/\eta + \delta_{DAC}^{SJ}(\nu T_s/\eta))] / (T_s/\eta)} \quad (3)$$

$$y_{\nu'} = \sum_{\nu=-N_{cp}}^{\eta N-1} s_{\nu} \frac{\sin(\pi [(\nu' T_s/\eta + \delta_{ADC}^{SJ}(\nu' T_s/\eta)) - (\nu T_s/\eta + \delta_{DAC}^{SJ}(\nu T_s/\eta))] / (T_s/\eta))}{\pi [(\nu' T_s/\eta + \delta_{ADC}^{SJ}(\nu' T_s/\eta)) - (\nu T_s/\eta + \delta_{DAC}^{SJ}(\nu T_s/\eta))] / (T_s/\eta)} \quad (6)$$

$$Y_l = \sum_{\nu'=0}^{\eta N-1} \left(\sum_{\nu=-\eta N_{cp}}^{\eta N-1} x_{\nu} \frac{\sin(\pi [(\nu' - \nu) T_s/\eta + (\delta_{ADC}^{SJ}(\nu' T_s/\eta) - \delta_{DAC}^{SJ}(\nu T_s/\eta))] / (T_s/\eta))}{\pi [(\nu' - \nu) T_s/\eta + (\delta_{ADC}^{SJ}(\nu' T_s/\eta) - \delta_{DAC}^{SJ}(\nu T_s/\eta))] / (T_s/\eta)} \right) e^{j2\pi l \nu' / (\eta N)} \quad (8)$$

$$\frac{\sin(\omega[(\nu' - \nu)T_s/\eta + (\delta_{\text{ADC}}^{\text{SJ}}(\nu'T_s/\eta) - \delta_{\text{DAC}}^{\text{SJ}}(\nu T_s/\eta))])}{\omega[(\nu' - \nu)T_s/\eta + (\delta_{\text{ADC}}^{\text{SJ}}(\nu'T_s/\eta) - \delta_{\text{DAC}}^{\text{SJ}}(\nu T_s/\eta))]} \quad (9)$$

$$\frac{\sin(\pi(\nu' - \nu))}{\pi(\nu' - \nu)} - \left(\frac{\pi(\nu' - \nu)\cos(\pi(\nu' - \nu)) - \sin(\pi(\nu' - \nu))}{\pi^2(\nu' - \nu)^2} \right) \omega(\delta_{\text{ADC}}^{\text{SJ}}(\nu'T_s/\eta) - \delta_{\text{DAC}}^{\text{SJ}}(\nu T_s/\eta)) \quad (10)$$

$$\varphi(\nu, \nu') = \begin{cases} 1, & \nu' = \nu \\ \frac{\cos(\pi(\nu' - \nu))}{\pi(\nu' - \nu)} \omega(\delta_{\text{ADC}}^{\text{SJ}}(\nu'T_s/\eta) - \delta_{\text{DAC}}^{\text{SJ}}(\nu T_s/\eta)), & \nu' \neq \nu \end{cases} \quad (11)$$

$$Y_l = X_l + \sum_{\nu'=0}^{\eta N-1} \left(\sum_{\nu=-N_{\text{CP}}, \nu \neq \nu'}^{\eta N-1} x_\nu \frac{\cos(\pi(\nu' - \nu))}{\pi(\nu' - \nu)} \omega(\delta_{\text{ADC}}^{\text{SJ}}(\nu'T_s/\eta) - \delta_{\text{DAC}}^{\text{SJ}}(\nu T_s/\eta)) \right) e^{j2\pi\nu' l / (\eta N)} \quad (12)$$

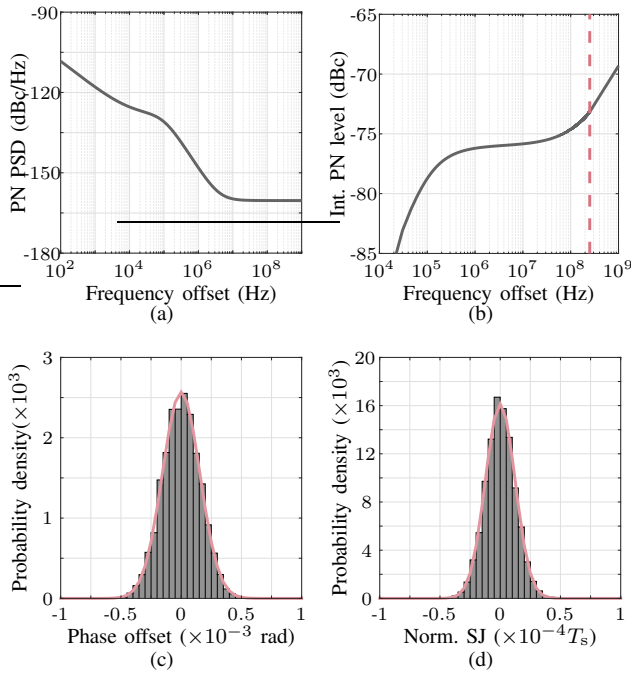


Fig. 1. Adopted PN model based on the Texas Instruments LMX2594 RF synthesizer [47]. The double-sided PN PSD is shown in (a), while the integrated PN level as a function of frequency offset (double-sided) for the frequency range of interest assuming BB sampling and $\eta = 1$ is presented in (b). In (b), $B/2 = 250$ MHz is highlighted (—), as this offset corresponds to the bandwidth $B = 500$ MHz listed in Table I. Finally, the PDF of the PN time series is shown in (c) and the corresponding SJ PDF in (d). Since a critical sampling period of $T_s = 2$ ns was considered, the PDF in (d) is associated with an RMS SJ of 49.44 fs.

which were assumed to be the same for both DAC and ADC, were 10^{-14} s, 10^{-13} s, 10^{-12} s, 10^{-11} s, and 10^{-10} s. Since $T_s = 1/B = 2$ ns, these numbers correspond to $0.5 \times 10^{-5} T_s$, $0.5 \times 10^{-4} T_s$, $0.5 \times 10^{-3} T_s$, $0.5 \times 10^{-2} T_s$, and $0.5 \times 10^{-1} T_s$, respectively. It can be seen in Fig. 2(a) that all considered parameterizations result in the same EVM of 24.13 dB. When $\eta = 2$ is adopted in Fig. 2(b), a significantly improved EVM is obtained in comparison to the case for $\eta = 1$ in Fig. 2,

especially for RMS SJ values equal to or smaller than 10^{-11} s (i.e., $0.5 \times 10^{-2} T_s$). When the oversampling factor is further increased to $\eta = 4$, an improvement of around 2 dB or less for $N \leq 1024$ is observed for an RMS SJ of 10^{-11} s. For RMS SJ values equal to or lower than 10^{-12} s, an improvement of up to 3 dB is observed for the whole considered N range. As for the oversampling factor $\eta = 8$, similar performance to the case with $\eta = 4$ is experienced, with exception for RMS SJ values equal to or lower than 10^{-12} s (i.e., $0.5 \times 10^{-3} T_s$). At the aforementioned SJ levels, up to around 1.4 dB higher EVM is experienced with $\eta = 8$. This is due to the fact that the experienced deviations from the correct sampling points are more relevant in this case than for $\eta = 4$, where the two times higher oversampled sampling period is experienced, i.e., $T_s^\eta = T_s/4$ instead of $T_s^\eta = T_s/8$. This result aligns the fact that colored makes oversampling less effective against the SJ than it would be in a case with white DAC and ADC SJ.

For all oversampling factors other than $\eta = 1$, i.e., $\eta \in \{2, 4, 8\}$, increasing the number of subcarriers N tends to result in lower EVM for RMS SJ equal to or lower than 10^{-11} s (i.e., $0.5 \times 10^{-2} T_s$). This is due to the smaller subcarrier spacing $\Delta f = B/N$, which leads to a more pronounced ICI effect and less relevant CPE. Since, however, ICI is rather low for these RMS SJ values, the greater robustness against CPE with increasing N stands out. In addition, an EVM degradation along with N of between approximately 13 dB and 15 dB is experienced between the RMS SJ values of 10^{-11} s and 10^{-10} s (i.e., $0.5 \times 10^{-2} T_s$ and $0.5 \times 10^{-1} T_s$), showing that the RMS SJ point where performance degradation starts becoming relevant lies between these two values. At this point, one relevant factor for performance degradation is the fact that increasing DAC SJ leads to increased OOB radiation [41], which will ultimately result in additional ICI after sampling at an ADC also impaired by SJ.

To illustrate the influence of DAC and ADC SJ on the receive constellations, Fig. 3 shows normalized QPSK constellations obtained with the transmission of OFDM symbols with $N \in \{256, 2048, 16384\}$, $N_{\text{CP}} = 0$ since an ideal channel is

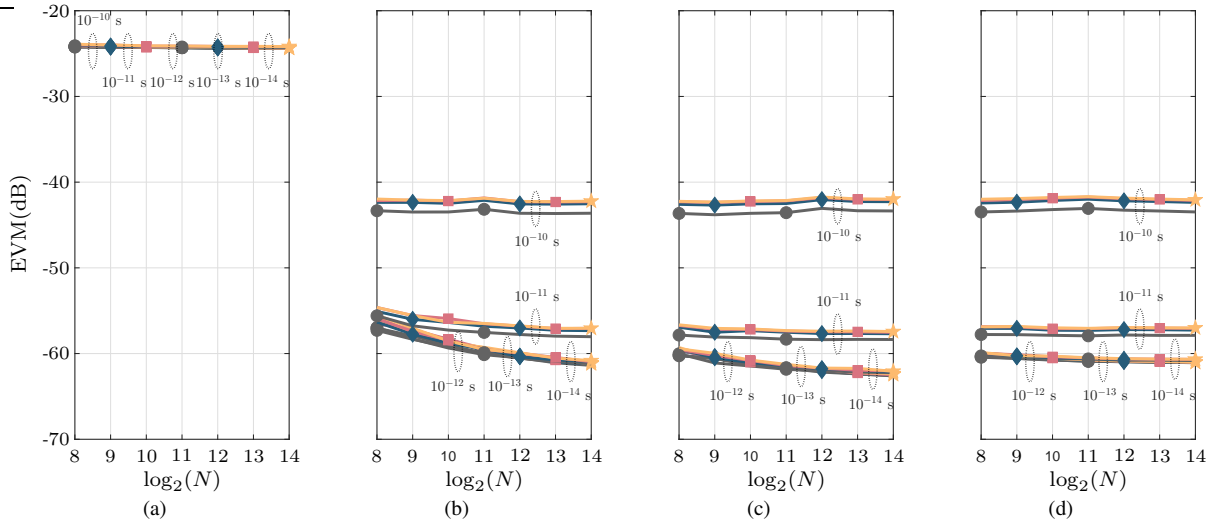


Fig. 2. Mean EVM obtained with BB sampling as a function of the number of subcarriers N . The performed simulations considered $M = 128$ OFDM symbols, and SJ RMS values of 10^{-14} s, 10^{-13} s, 10^{-12} s, 10^{-11} s, and 10^{-10} s at both transmitter and receiver. These values correspond to RMS SJs of $0.5 \times 10^{-5}T_s$, $0.5 \times 10^{-4}T_s$, $0.5 \times 10^{-3}T_s$, $0.5 \times 10^{-2}T_s$, and $0.5 \times 10^{-1}T_s$, respectively. In addition, quadrature phase-shift keying (QPSK) (●), 16-quadrature amplitude modulation (QAM) (◆), 64-QAM (■), and 256-QAM (★) modulations were considered. For the results in (a), (b), (c), and (d), $\eta = 1$, $\eta = 2$, $\eta = 4$, and $\eta = 8$ were used, respectively.

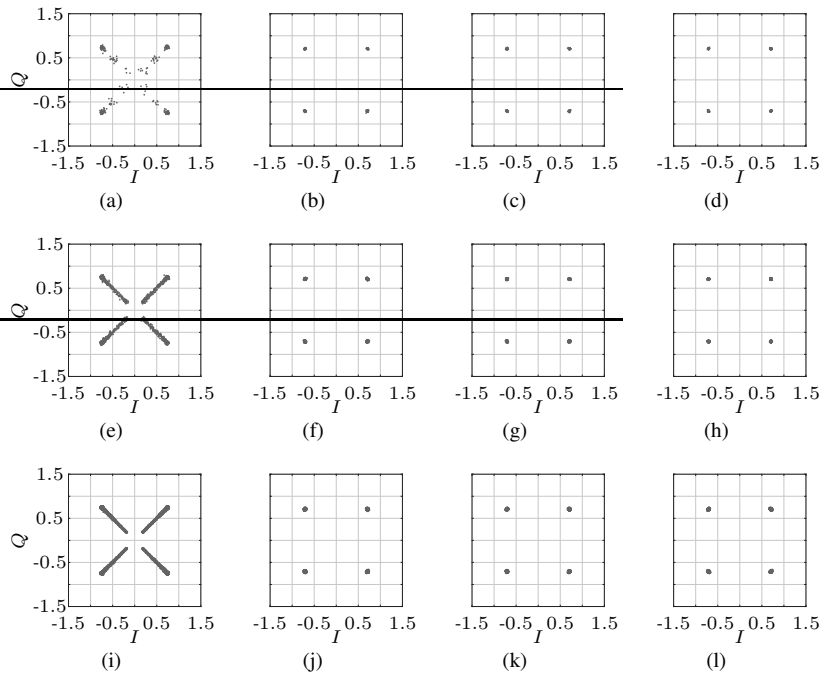


Fig. 3. Normalized receive QPSK constellations obtained with BB sampling, $M = 128$ OFDM symbols, and an RMS SJ of 10^{-10} s (i.e., $0.5 \times 10^{-1}T_s$). Results are shown for different numbers of subcarriers and zero padding (ZP) factors, namely $N = 256$ and (a) $\eta = 1$, (b) $\eta = 2$, (c) $\eta = 4$, (d) $\eta = 8$, $N = 2048$ and (e) $\eta = 1$, (f) $\eta = 2$, (g) $\eta = 4$, (h) $\eta = 8$, and $N = 16384$ and (i) $\eta = 1$, (j) $\eta = 2$, (k) $\eta = 4$, (l) $\eta = 8$.

assumed, and $\eta \in \{1, 2, 4, 8\}$. For all cases, $M = 128$ OFDM symbols and an RMS SJ of 10^{-10} s (i.e., $0.5 \times 10^{-1}T_s$) were considered. The obtained constellations confirm that the highest EVM values are observed for $\eta = 1$, besides an increasing EVM trend from $\eta = 2$ to $\eta = 8$, while N plays no significant role. While this would be different for lower RMS SJ values as previously discussed, rather low EVM values would be experienced and their effect would not be clearly visible in the QPSK constellations. To enable a better understanding of the mean EVM behavior and the

constellation shapes, Fig. 4 shows the EVM per subcarrier for the same parameters assumed for the results presented in Fig. 3. The obtained results reveal that $\eta = 1$ results in pronounced distortion at the edge subcarriers due to the use of the critical sampling frequency. It can also be seen that the EVM pattern is clearly improved with oversampling factors $\eta \in \{2, 4, 8\}$. The obtained values are still frequency-selective, which, however, is due to the considered colored SJ. As expected from the results in Fig. 2 for the RMS SJ of 10^{-10} s, no significant difference is observed for different N

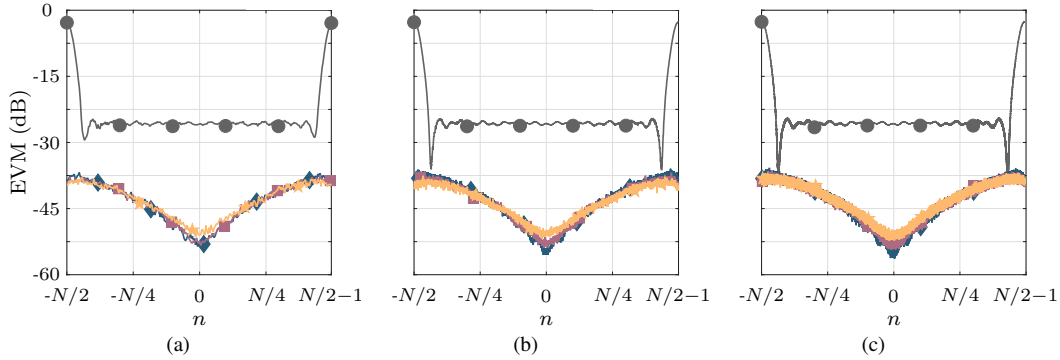


Fig. 4. EVM at the n th subcarrier obtained with BB sampling and an RMS SJ of 10^{-10} s (i.e., $0.5 \times 10^{-1}T_s$), QPSK modulation, and: (a) $N = 256$, (b) $N = 2048$, and (c) $N = 16384$. In all cases, results are shown for $\eta = 1$ (●), $\eta = 2$ (◆), $\eta = 4$ (■), and $\eta = 8$ (★).

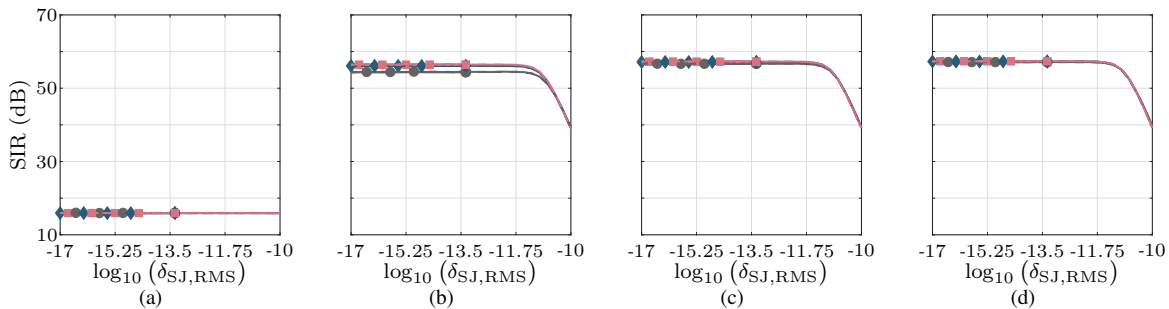


Fig. 5. SIR as a function of the RMS SJ obtained with BB sampling, $M = 128$ OFDM symbols, QPSK modulation, and (a) $\eta = 1$, (b) $\eta = 2$, (c) $\eta = 4$, and (d) $\eta = 8$. In all cases, results are shown for $N = 256$ (●), $N = 2048$ (◆), and $N = 16384$ (■).

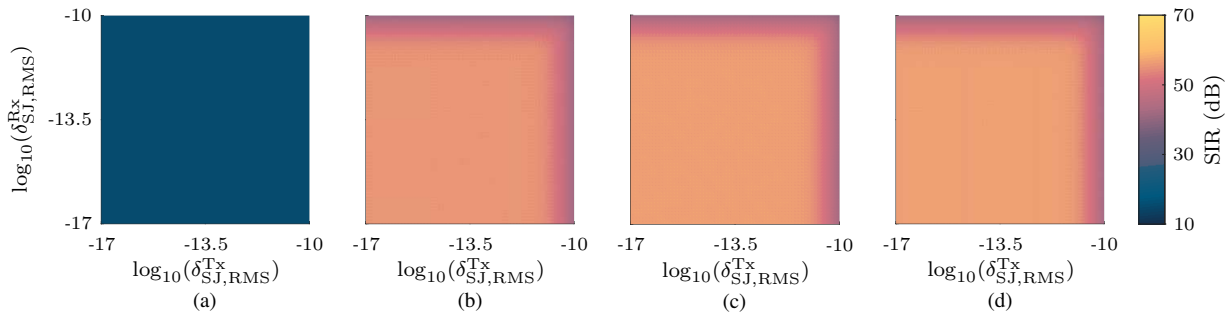


Fig. 6. SIR obtained with BB sampling, $M = 128$ OFDM symbols, QPSK modulation, and different RMS SJ values at the DAC and ADC. Results are shown for $N = 2048$ and (a) $\eta = 1$, (b) $\eta = 2$, (c) $\eta = 4$, and (d) $\eta = 8$.

values for the considered RMS SJ value.

To further quantify the SJ-induced communication performance degradation in the considered OFDM-based ISAC system, Fig. 5 shows the obtained SIR as a function of the RMS SJ, which is assumed to be equal at both DAC and ADC. For the performed simulations, the same numbers of subcarriers N , CP length, number of OFDM symbols, digital modulation schemes, and oversampling factors was adopted as for the results in Figs. 3 and 4, i.e., $N \in \{256, 2048, 16384\}$, $N_{CP} = 0$, $M = 128$, QPSK and $\eta \in \{1, 2, 4, 8\}$. The achieved results show a constant SIR of 15.92 dB for $\eta = 1$ regardless of the number of subcarriers N , which is mainly due to the severe distortion of the edge subcarriers. For $\eta = 2$, in turn, a maximum SIR of around 56.44 dB is observed, whereas $\eta = 4$ and $\eta = 8$ yield maximum SIR values of approximately 57.27 dB

and 57.33 dB, respectively. The obtained results agree with the fact that oversampling has limited effectiveness against ADC SJ and the OOB radiation due to DAC SJ, as previously discussed in Section II. With increasing RMS SJ after 10^{-11} s (i.e., $0.5 \times 10^{-12}T_s$), however, the performance of the cases with higher η among $\eta \in \{2, 4, 8\}$ tend to start degrading. In addition, slightly higher robustness against increasing RMS SJ is observed for a higher number of subcarriers N for these oversampling factors, as was the case in the previous EVM analyses. Next, Fig. 6 shows the obtained SIR considering different RMS SJ values for the DAC and the ADC, $N = 2048$, and QPSK modulation. It can be seen that, apart from $\eta = 1$, which achieves the worst SIR performance at low RMS SJs, a slight SIR improvement is observed when increasing η from 2 to 4, but no further noticeable enhancement is observable

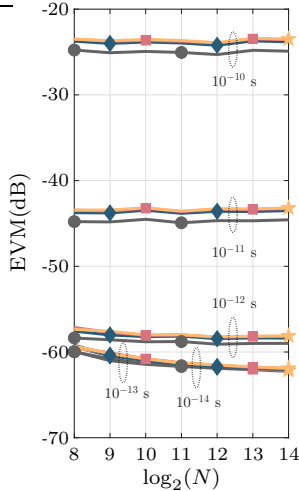


Fig. 7. Mean EVM obtained with BP sampling at a digital IF $f_{IF} = 1$ GHz as a function of the number of subcarriers N . For the obtained results, $\eta = 8$, $M = 128$ OFDM symbols, and SJ RMS values of 10^{-14} s, 10^{-13} s, 10^{-12} s, 10^{-11} s, and 10^{-10} s (i.e., $0.5 \times 10^{-5}T_s$, $0.5 \times 10^{-4}T_s$, $0.5 \times 10^{-3}T_s$, $0.5 \times 10^{-2}T_s$, and $0.5 \times 10^{-1}T_s$, respectively) at both the DAC and the ADC were considered. As in Fig. 2, QPSK (●), 16-QAM (◆), 64-QAM (■), and 256-QAM (★) modulations were considered.

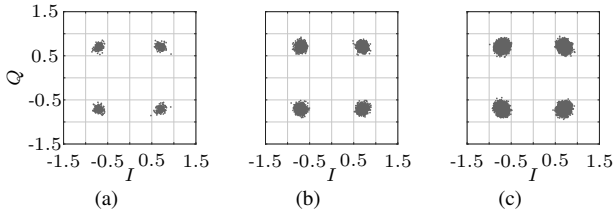


Fig. 8. Normalized receive QPSK constellations obtained with BP sampling at a digital IF $f_{IF} = 1$ GHz, $\eta = 8$, $M = 128$ OFDM symbols, and an RMS SJ of 10^{-10} s (i.e., $0.5 \times 10^{-1}T_s$) at both the DAC and the ADC. Results are shown for (a) $N = 256$, (b) $N = 2048$, and (c) $N = 16384$ total number of subcarriers.

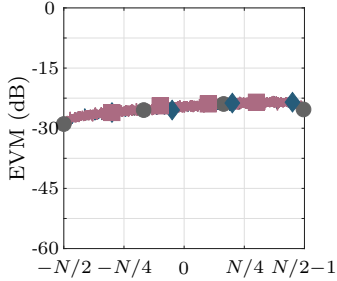


Fig. 9. EVM at the n th subcarrier obtained with BP sampling at a digital IF $f_{IF} = 1$ GHz, $\eta = 8$, $M = 128$ OFDM symbols, QPSK modulation and an RMS SJ of 10^{-10} s (i.e., $0.5 \times 10^{-1}T_s$) at both the DAC and the ADC. Results are shown for $N = 256$ (●), $N = 2048$ (◆), and $N = 16384$ (■) total number of subcarriers.

for $\eta = 8$, which supports the previous results. In addition, the obtained results reveal that the adopted colored SJ model leads to similar effects when applied at either DAC or ADC, which agrees with the result from (12).

B. Bandpass Sampling

In BP sampling, the transmit signal must first undergo oversampling before DUC to the digital IF. The inverse is done at

the receiver side, i.e., DDC followed by downsampling. In this subsection, a digital IF of $f_{IF} = 1$ GHz and an oversampling factor $\eta = 8$ used during FDZP are adopted to analyze the effect of SJ on the communication performance of an OFDM-based ISAC system with BP sampling. Given these parameters, Fig. 7 shows the achieved mean EVM as a function of the number of subcarriers for the same digital modulations and RMS SJ values considered for the results for BB sampling in Fig. 2. Compared to the results for $\eta = 8$ in the BB sampling case, considerably higher EVM values are achieved with BP sampling.

The aforementioned results are illustrated by the normalized receive QPSK constellations in Fig. 8 for the RMS SJ of 10^{-10} s (i.e., $0.5 \times 10^{-1}T_s$). The observed results show no difference in the constellations densities for different N as expected from Fig. 7. Only less points are seen for $N = 14$ as the same number of OFDM symbols, i.e., $M = 128$, was assumed in all cases. Compared to the constellations in the BB case with $\eta = 8$ in Fig. 3, a clear degradation of the constellation is observed both in the form of spreading due to ICI and slight rotation of some points due to CPE, which is mainly due to two factors. The first is the more severe ICI effect, as the OFDM signal is transmitted at higher frequencies where the PN PSD from which the SJ is derived has accumulated a higher level as seen in Fig. 1b. The second factor, which is the source of the constellation rotation, is the CPE that is experienced due to the PN-like effect induced by the SJ on the digital IF used to transmit the OFDM signal as discussed in [38]. These results are linked to the ones in Fig. 9, where the obtained EVM per subcarrier for the same signal parameters are shown. Unlike the results for BB sampling in Fig. 4, a smaller EVM variation with an overall higher level is observed in all cases with BP sampling, which is due to the aforementioned accumulated PN level at that region and SJ-induced CPE to the digital IF.

Next, Fig. 10 shows the experienced SIR as a function of the RMS SJ for QPSK modulation and the same remaining signal parameters assumed for the results in Figs. 8 and 9. The obtained results show that a maximum SIR of around 55.82 dB is achieved for all considered N values, which is around 1.51 dB lower than in the BB sampling case with $\eta = 8$ in Fig. 5(d). If CPE estimation and correction is performed, e.g., as described in [36], the SIR is improved by only around 0.57 dB for RMS SJs above 10^{-11} s (i.e., $0.5 \times 10^{-2}T_s$), which is where the SIR starts degrading. The reason for this is that, when CPE becomes relevant, the ICI induced by SJ is already severe enough to impair the CPE estimation and make its correction less effective. Results assuming different RMS SJ values at the DAC and ADC are finally shown for a reduced RMS SJ range in Fig. 11 for the cases with and without CPE compensation. As in the BB sampling case for $\eta = 8$ in Fig. 6(d), similar effects are observed for both DAC and ADC SJs. With BP sampling, however, a significant SIR degradation is experienced as previously discussed, and the CPE correction presents the same slight SIR improvement of only around 0.57 dB for RMS SJs above 10^{-11} s. This allows concluding that, for the adopted colored SJ model, ICI is the dominant impairment induced by SJ.

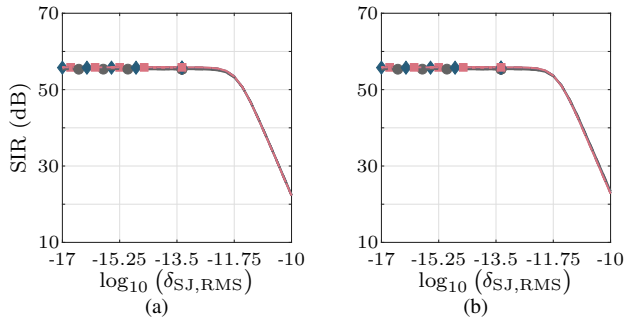


Fig. 10. SIR as a function of the RMS SJ (same at both the DAC and the ADC) obtained with BP sampling at a digital IF $f_{IF} = 1$ GHz, $\eta = 8$, and $M = 128$ OFDM symbols (a) without and (b) with CPE correction. In all cases, results are shown for $N = 256$ (●), $N = 2048$ (◆), and $N = 16384$ (■), as well as QPSK (—) and 256-QAM (—) modulations. In the obtained results, an SIR improvement of only around 0.57 dB is seen when CPE compensation is performed. In addition, no significant difference is observed between the experienced SIR with QPSK and 256-QAM.

C. Remarks on simulation results

As evidenced by the obtained expressions (12) and (13), besides related studies in the literature, it was shown that SJ exclusively causes ICI if BB sampling is adopted. If BP sampling is adopted instead, SJ also leads to CPE and additional ICI due to a PN-like effect on the digital IF. Consequently, BP tends to result in more severely degraded communication performance, yielding higher EVM and SIR than in the BB case as the receive constellations are not only spread due to ICI, but also rotated due to CPE. It was also shown that the absence of oversampling in the BB sampling case, i.e., $\eta = 1$, leads to the distortion of the edge subcarriers and therefore the highest EVM and lowest SIR. While performing oversampling prevents that issue, the results have shown that adopting increasing oversampling factors among the considered values $\eta \in \{2, 4, 8\}$ only leads to improvement at rather low RMS SJ at both DAC and ADC. For higher RMS SJ, however, more significant OOB radiation due to DAC SJ happens, which combined with the ICI induced by both DAC and ADC SJ, leads to more degraded communication performance, both in terms of EVM and SIR, than with a lower oversampling factor among the considered ones. Finally, it can be concluded that RMS SJ values of up to around 10^{-10} s (i.e., $0.5 \times 10^{-1} T_s$) at both DAC and ADC result in tolerable communication performance degradation for BB sampling with all considered oversampling factors, ensuring EVM below -40 dB and maximum SIR of around 56 dB to 57 dB. The reason why better values are not obtained with even lower RMS SJ values is due to limited accuracy in the SJ simulation, which is done with via resampling with a Farrow filter [50] preceded by cubic interpolation [51]. For the BP sampling scenario at an IF of $f_{IF} = 1$ GHz and with oversampling $\eta = 8$, the same RMS SJ upper bound applies.

IV. NUMERICAL RESULTS FOR RADAR SENSING

In this section, the effects of SJ on radar sensing in OFDM-based ISAC systems is analyzed. For that purpose, the same SJ model from Section III is adopted. To analyze how the EVM and SIR degradation ultimately translate into degradation

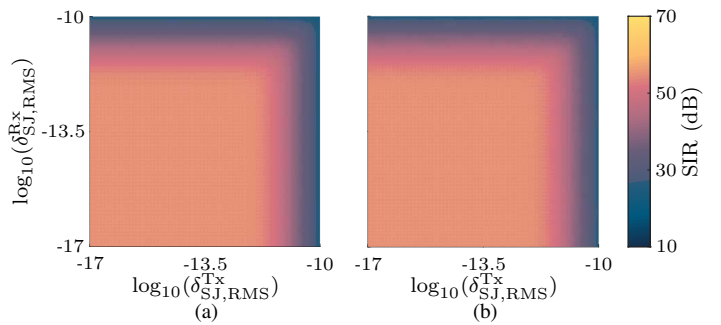


Fig. 11. SIR as a function of the RMS SJ (same at both the DAC and the ADC) obtained with BP sampling at a digital IF of $f_{IF} = 1$ GHz, $\eta = 8$, $N = 2048$ subcarriers, and $M = 128$ OFDM symbols, and QPSK modulation (a) without and (b) with CPE correction. As in Fig. 10, only around only around 0.57 dB SIR improvement due to CPE compensation was observed.

of target reflections in a radar image, several performance parameters are used. These include PPLR, PSLR, and ISLR [7], [52], [53], as well as SIR [36]. To better understand the effects of SJ, the PSLR and ISLR parameters are evaluated for both range and Doppler shift directions of the simulated radar images. Finally, SIR is used as a measure of the ratio between a target peak and the interference floor raised by SJ in the radar image.

The obtained results assuming BB and BP sampling are discussed in Sections IV-A and IV-B, respectively, with remarks on the presented simulation results given in Section IV-C. For the performed simulations, the parameters from Table I are considered. For conciseness, however, only $N \in \{256, 2048, 16384\}$, besides QPSK and 256-QAM are henceforth considered. In addition, a scenario with a single static target was considered and all other typical impairments in OFDM-based ISAC systems such as additive white Gaussian noise (AWGN), external interference and self-interference are not considered to focus on the SJ effects. Since the assumed SJ model is uncorrelated in both monostatic and bistatic ISAC architectures, the same degradation due to SJ is experienced in both cases. Therefore, the following radar sensing performance analyses assume a bistatic OFDM-based ISAC with perfect synchronization and full knowledge of the transmit OFDM frame for radar signal processing. Finally, the same SJ is assumed for both DAC and ADC. This is done since, as also demonstrated in [42] and by the results in Section III, both DAC and ADC SJ yield the same effects. The expression in (12) also confirms this, showing that the combined DAC and ADC SJ is the defining factor for the OFDM-based ISAC system performance.

A. Baseband Sampling

Assuming BB sampling for the considered OFDM-based ISAC system, PPLR, range and Doppler shift PSLR, as well as range and Doppler shift ISLR were calculated as functions of the normalized RMS SJ values between 10^{-17} s and 10^{-10} s (i.e., $0.5 \times 10^{-8} T_s$ and $0.5 \times 10^{-1} T_s$, respectively) for oversampling factors $\eta \in \{1, 2, 4, 8\}$. In the performed simulations, the considered RMS SJ values were assumed to be equal at both DAC and ADC, and only rectangular windowing was

TABLE II

SIMULATED PPLR, RANGE AND DOPPLER SHIFT PSLR, AND RANGE AND DOPPLER SHIFT ISLR FOR BB SAMPLING AND RMS SJ BETWEEN 10^{-17} s AND 10^{-10} s ($0.5 \times 10^{-8}T_s$ AND $0.5 \times 10^{-1}T_s$)

η	PPLR	Range PSLR (dB)	Doppler PSLR (dB)	Range ISLR (dB)	Doppler ISLR (dB)
1	0 dB	-13.44 dB	-13.30 dB	-10.84 dB	-9.68 dB
2	0 dB	-13.30 dB	-13.30 dB	-9.68 dB	-9.68 dB
4	0 dB	-13.30 dB	-13.30 dB	-9.69 dB	-9.68 dB
8	0 dB	-13.27 dB	-13.30 dB	-9.67 dB	-9.68 dB

performed during both range and Doppler processing. Since negligible difference between QPSK and 256-QAM, among different N values, and for different RMS SJ values within the considered range was observed, the obtained results are shown in Table II as a function of the oversampling factor η only. The obtained results show negligible PPLR for all cases, and similar overall performance. The most pronounced differences, which are still rather small, are observed in the for range PSLR and ISLR with $\eta = 1$. With this oversampling factor, the worst values are achieved due to the distortion of the edge subcarriers even with low RMS SJ. It is worth highlighting that, since CPE due to SJ is not experienced in the BB sampling case and the fixed number $M = 128$ of OFDM symbols is assumed, the same Doppler shift PSLR and ISLR is observed in all cases.

While PPLR, PSLR, and ISLR do not clearly showcase the influence of SJ on the radar sensing performance, the SIR distinctly captures this effect as illustrated in Fig. 12. This figure shows the achieved mean and minimum image SIR as a function of the RMS SJ. These parameters are defined as the average and minimum power ratio, respectively, that is calculated between the target peak and each point outside the mainlobe. The performed simulations assumed equal RMS SJ at both DAC and ADC, as well as the remaining parameters used for the previously discussed PPLR, PSLR, and ISLR results. Overall, a better performance is obtained with QPSK compared to 256-QAM, with a more pronounced difference in the mean image SIR case ranging from 3 dB to 6 dB. In addition, increasing oversampling factors η and number of subcarriers N also result in higher SIR. While the first parameter is directly proportional to the processing gain experienced against the SJ-induced ICI after range processing. It can also be seen that the mean image SIR values are from around 12 dB to 37 dB higher than the minimum image SIR values, with exact values depending on η , N , and the modulation alphabet. This is due to the SJ-induced ICI, which may lead to artifacts that cannot be always suppressed by windowing as later shown in the results in Figs. 13 and 14. For all considered η values, the SIR values only start degrading at RMS SJ equal to or higher than 10^{-11} s (i.e., $0.5 \times 10^{-2}T_s$), which was also the case in the communication analysis in Section III. Unlike in the communication case, a more pronounced image SIR improvement is observed when increasing the oversampling factor from $\eta = 2$ to $\eta = 4$, and from $\eta = 4$ to $\eta = 8$. This is particularly visible for mean SIR with $N \in \{256, 2048\}$ (comparing Figs. 12(b) and 12(c)) in the former case, and with $N \in \{256\}$ (comparing Figs. 12(c) and 12(d)) in the latter. In addition, the fact that maximum

TABLE III

SIMULATED PPLR, RANGE AND DOPPLER SHIFT PSLR, AND RANGE AND DOPPLER SHIFT ISLR FOR BP SAMPLING AND RMS SJ BETWEEN 10^{-17} s AND 10^{-10} s ($0.5 \times 10^{-8}T_s$ AND $0.5 \times 10^{-1}T_s$)

η	PPLR	Range PSLR (dB)	Doppler PSLR (dB)	Range ISLR (dB)	Doppler ISLR (dB)
8	0 dB	-13.33 dB	-13.30 dB	-9.70 dB	-9.68 dB

observed mean SIR is limited at around 136 dB, as seen for $N = 16384$ and QPSK modulation in Fig. 12(b), (c), and (d)) is due to the previously discussed limited accuracy in the SJ simulation.

To illustrate the influence of the degradation of the previously analyzed parameter on obtained radar images, Figs. 13 and 14 show obtained bistatic range-Doppler radar images with $\eta = 1$ and $\eta = 8$, respectively. Further considered parameters are $N = 2048$, $N_{CP} = 2048$, $M = 128$, and QPSK. In addition, two targets were simulated. The first was at 10 m with a Doppler shift of 0 kHz, and the second at 15 m with a Doppler shift of $0.1\Delta f$. In both figures, radar images are shown for the cases where rectangular windowing or Chebyshev windowing with 100 dB sidelobe suppression are adopted for both range and Doppler shift processing, with RMS SJ values at both DAC and ADC of 10^{-16} s, 10^{-13} s, and 10^{-10} s (i.e., $0.5 \times 10^{-7}T_s$, $0.5 \times 10^{-4}T_s$, and $0.5 \times 10^{-1}T_s$, respectively) for both cases. While rectangular windowing results in high range and Doppler shift sidelobes, which partly mask the effect of SJ as illustrated by the previously presented discussion on PPLR, PSLR and ISLR results, Chebyshev windowing allows clearly observing the expected SIR degradation along with increasing RMS SJ as previously seen in Fig. 12.

B. Bandpass Sampling

For the case where BP sampling is performed at a digital IF of $f_{IF} = 1$ GHz with oversampling factor $\eta = 8$, Table III shows the simulated PPLR, range and Doppler shift PSLR, as well as range and Doppler shift ISLR. Simulations were performed for both QPSK and 256-QAM, $N \in \{256, 2048, 16384\}$ and $M = 128$, within the RMS SJ range from 10^{-17} s to 10^{-10} s (i.e., $0.5 \times 10^{-8}T_s$ to $0.5 \times 10^{-1}T_s$, respectively). As in the BB case in Section IV-B, negligible differences between all these settings was observed, which is why a single result is shown for each performance parameter. Compared to the BB results for $\eta = 8$ in Table II, only negligible differences of 0.06 dB and 0.03 dB were observed in range PSLR and ISLR, respectively.

Next, the mean and minimum image SIR obtained as a function of the RMS SJ are shown in Figs. 15(a) and 15(b), respectively. Since negligible improvement is experienced with CPE correction as previously demonstrated by the results in Fig. 10, only results without CPE correction are shown. As in the BB case in Fig. 12, equal RMS SJ was assumed for both DAC and ADC, and the same set of parameters except for a fixed oversampling factor $\eta = 8$ is adopted. Overall, a similar behavior as in the BB case with $\eta = 8$ is observed, i.e., higher N yields higher image SIR and QPSK outperforms

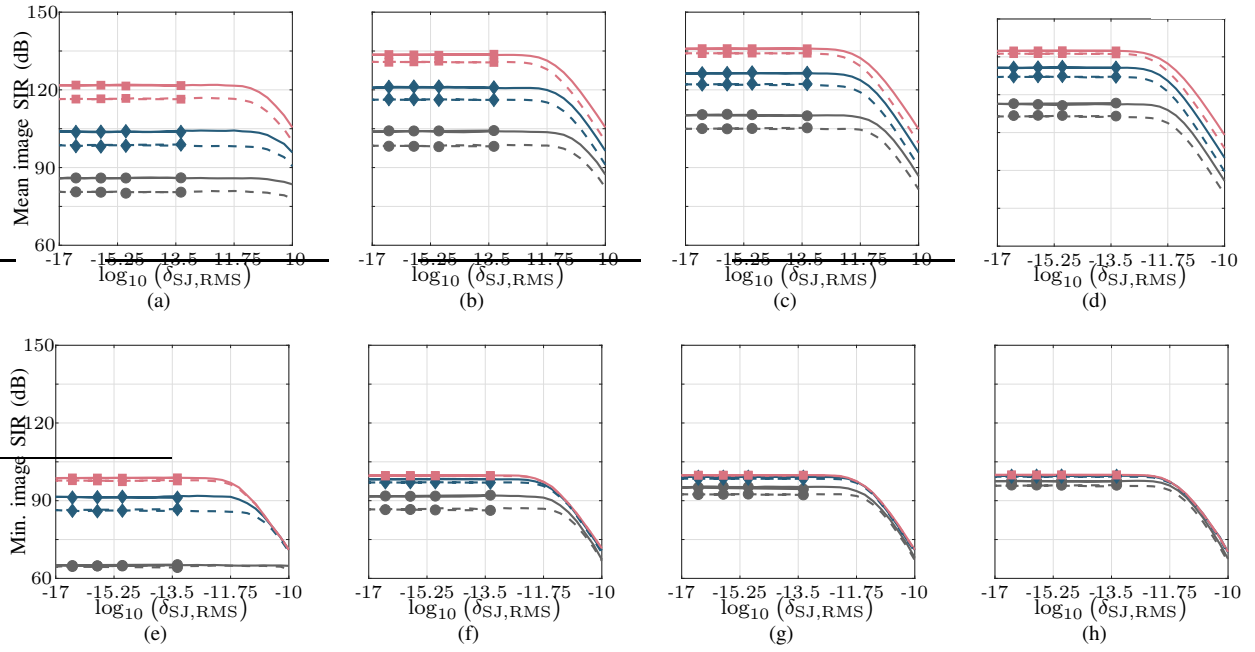


Fig. 12. Image SIR as a function of the normalized RMS SJ by the critical sampling period T_s (same at both the DAC and the ADC) jitter obtained with BB sampling, $M = 128$ OFDM symbols. The simulated mean image SIR is shown for (a) $\eta = 1$, (b) $\eta = 2$, (c) $\eta = 4$, and (d) $\eta = 8$, while the simulated minimum image SIR is shown for the same η values in (e), (f), (g), and (h), respectively. In all cases, results are shown for $N = 256$ and QPSK (— and ●), $N = 2048$ and QPSK (— and ◆), and $N = 16384$ and QPSK (— and ●), as well as $N = 256$ and 256-QAM (— and ●), $N = 2048$ and 256-QAM (— and ◆), and $N = 16384$ and 256-QAM (— and ■).

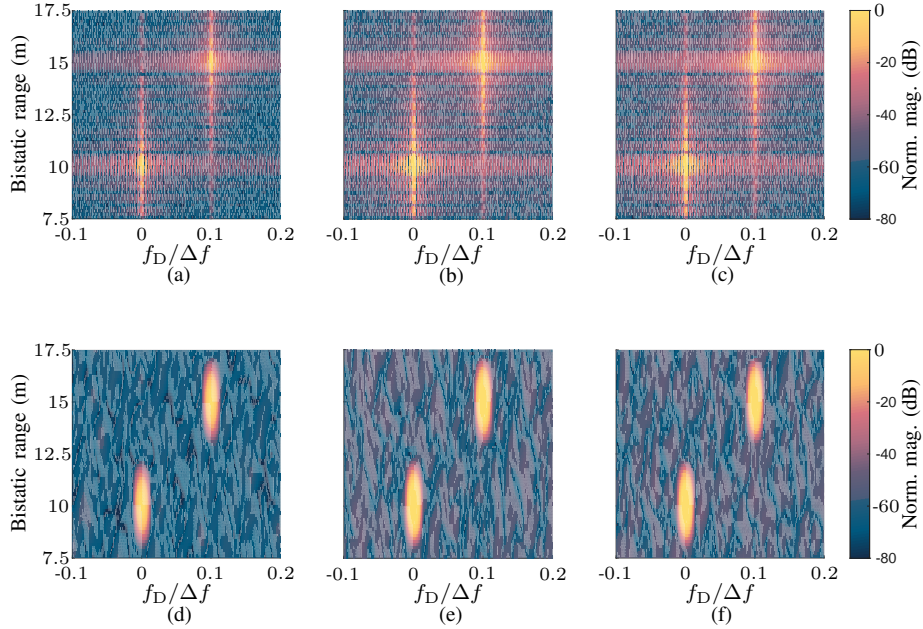


Fig. 13. Bistatic range-Doppler radar images obtained with BB sampling, $N = 2048$, $N_{CP} = 2048$, $M = 128$, QPSK modulation, and $\eta = 1$. A target at 10 m with a Doppler shift of 0 kHz and another at 15 m with a Doppler shift of $0.1\Delta f$ were simulated. Results are shown for rectangular windowing for both range and Doppler shift processing and RMS SJ values at both DAC and ADC of (a) 10^{-16} s, (b) 10^{-13} s, and (c) 10^{-10} s (i.e., $0.5 \times 10^{-7}T_s$, $0.5 \times 10^{-4}T_s$, and $0.5 \times 10^{-1}T_s$, respectively), as well as for Chebyshev windowing with 100 dB sidelobe suppression for both range and Doppler shift processing and RMS SJ values at both DAC and ADC of (d) 10^{-16} s, (e) 10^{-13} s, and (f) 10^{-10} s.

256-QAM. Lower image SIR values are obtained in the BP sampling case due to the fact that CPE is experienced besides ICI. Comparing Fig. 15(a) with the BB sampling results from 12(d), lower mean image SIR values by 7.11 dB, 4.93 dB, and 1.79 dB are experienced considering QPSK modulation

and $N = 256$, $N = 2048$, and $N = 16384$, respectively. This aligns with the fact that lower N results in more pronounced CPE. For 256-QAM, these values are increased to 7.24 dB, 5.90 dB, and 2.36 dB as higher modulation order results in more severe effect for the same CPE. In terms of minimum

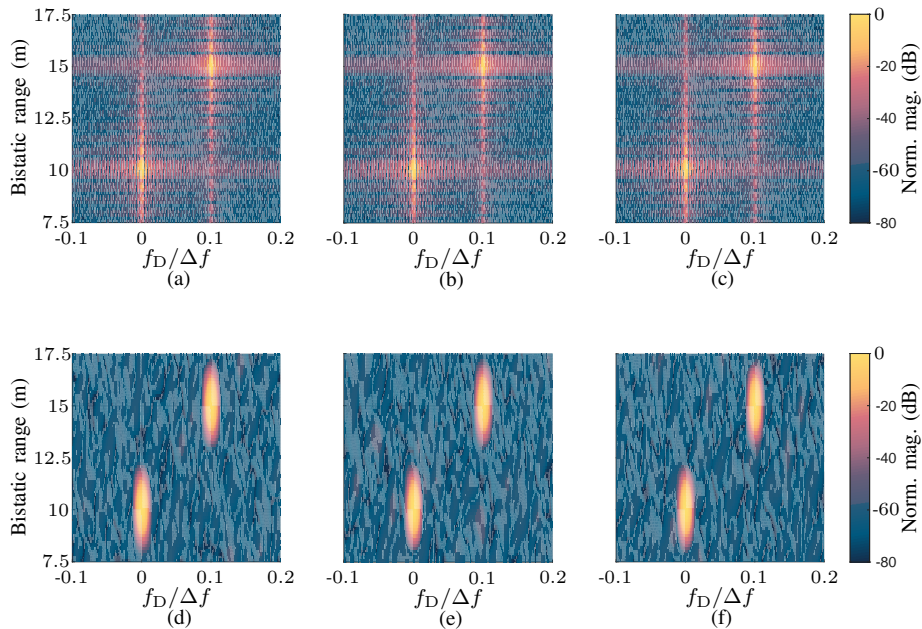


Fig. 14. Bistatic range-Doppler radar images obtained with BB sampling, $N = 2048$, $N_{CP} = 2048$, $M = 128$, QPSK modulation, and $\eta = 8$. The same targets as for the radar images shown in Fig. 13 were simulated. Results are shown for rectangular windowing for both range and Doppler shift processing and RMS SJ values at both DAC and ADC of (a) 10^{-16} s, (b) 10^{-13} s, and (c) 10^{-10} s (i.e., $0.5 \times 10^{-7}T_s$, $0.5 \times 10^{-4}T_s$, and $0.5 \times 10^{-1}T_s$, respectively), as well as for Chebyshev windowing with 100 dB sidelobe suppression for both range and Doppler shift processing and RMS SJ values at both DAC and ADC of (d) 10^{-16} s, (e) 10^{-13} s, and (f) 10^{-10} s.

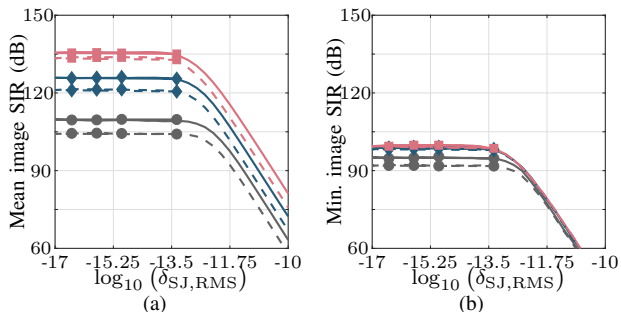


Fig. 15. Mean (a) and minimum (b) image SIR as a function of the normalized RMS SJ by the critical sampling period T_s (same at both the DAC and the ADC) jitter obtained with BP sampling at a digital IF $f_{IF} = 1$ GHz, $\eta = 8$, and $M = 128$ OFDM symbols. In all cases, results are shown for $N = 256$ and QPSK (— and ●), $N = 2048$ and QPSK (— and ◆), and $N = 16384$ and QPSK (— and ■), as well as $N = 256$ and 256-QAM (— and ●), $N = 2048$ and 256-QAM (— and ◆), and $N = 16384$ and 256-QAM (— and ■).

image SIR, however, a difference between the results for BP sampling shown in Fig. 15(b) are only worse than its BB counterparts from Fig. 12(d) for $N = 256$. More specifically, 2.32 dB, 3.59 dB lower values are obtained for QPSK and 256-QAM, respectively.

To show how the influence on radar images of the main lobe and sidelobe degradation measured by PPLR, PSLR, and ISLR, as well as the dynamic range reduction measured by the SIR, Fig. 16 shows simulated bistatic range-Doppler radar images with BP sampling at a digital IF of $f_{IF} = 1$ GHz and with $\eta = 8$. In addition, $N = 2048$, $N_{CP} = 2048$, $M = 128$, and QPSK modulation were considered. As for windowing, results are shown for both rectangular window and Chebyshev

window with 100 dB sidelobe suppression applied during both range and Doppler shift processing. The same two targets as for the BB case in Figs. 13 and 14 are considered, namely one at 10 m with a Doppler shift of 0 kHz, and the another at 15 m with a Doppler shift of $0.1\Delta f$. Furthermore, RMS SJ values of 10^{-16} s, 10^{-13} s, and 10^{-10} s (i.e., $0.5 \times 10^{-7}T_s$, $0.5 \times 10^{-4}T_s$, and $0.5 \times 10^{-1}T_s$, respectively) were considered, with the same value being adopted for both DAC and ADC at each simulation. The resulting range-Doppler shift radar images from simulations with the aforementioned parameters confirm the findings from the previous results on radar sensing with BP sampling in the considered OFDM-based ISAC system. More specifically, they show that both ICI and CPE strongly influence the quality of the obtained radar images, which become severely degraded at significantly lower RMS SJ than in the BB case. While the ICI can be suppressed to a certain extent due to the radar processing gain, the CPE effect is not effectively attenuated, leading to stripes in the Doppler shift direction at the range of the true targets. This is especially visible in Fig. 16(f) where 10^{-10} s RMS SJ and Chebyshev windowing were considered. Since, in contrast to the range sidelobes, these artifacts cannot be effectively suppressed by windowing, they can eventually lead to the detection of ghost targets.

C. Remarks on simulation results

The obtained results have shown that neither the main lobe, measured by PPLR, nor the range and Doppler shift sidelobes, measured by PSLR and ISLR, of a target in a radar image experience significant degradation for the considered RMS SJ range between 10^{-17} s and 10^{-10} s (i.e.,

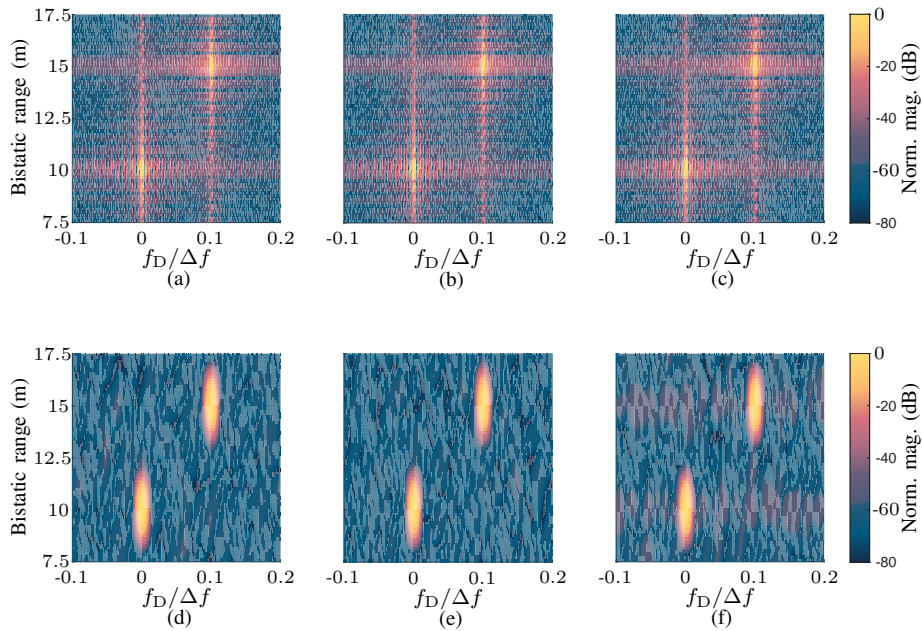


Fig. 16. Bistatic range-Doppler radar images obtained with BP sampling at a digital IF $f_{IF} = 1$ GHz, $N = 2048$, $N_{CP} = 2048$, $M = 128$, QPSK modulation, $\eta = 8$ and Chebyshev windowing with 100 dB sidelobe suppression for both range and Doppler shift processing. The same targets as for the radar images shown in Figs. 13 and 14 were simulated. Results are shown for rectangular windowing for both range and Doppler shift processing and RMS SJ values at both DAC and ADC of (a) 10^{-16} s, (b) 10^{-13} s, and (c) 10^{-10} s (i.e., $0.5 \times 10^{-7}T_s$, $0.5 \times 10^{-4}T_s$, and $0.5 \times 10^{-1}T_s$, respectively), as well as for and Chebyshev windowing with 100 dB sidelobe suppression for both range and Doppler shift processing and RMS SJ values at both DAC and ADC of (d) 10^{-16} s, (e) 10^{-13} s, and (f) 10^{-10} s.

$0.5 \times 10^{-8}T_s$ and $0.5 \times 10^{-1}T_s$, respectively) at both DAC and ADC for any of the considered numbers of subcarriers, i.e., $\eta \in \{256, 2048, 16384\}$, and oversampling factors, i.e., $\eta \in \{1, 2, 4, 8\}$, both for BB and BP sampling.

Although no relevant main or sidelobe degradation is measured by the PPLR, PSLR and ISLR parameters, it was shown that the described ICI and CPE effects lead to non-negligible image SIR degradation for RMS SJ above 10^{-11} s (i.e., $0.5 \times 10^{-2}T_s$). Notably, it was verified that the CPE in the BP sampling case may lead to stripes in the Doppler shift direction at the range of the true targets in the radar image. This can lead to ghost targets and, in scenarios with multiple targets, mask weaker target reflections.

V. CONCLUSION

This article analyzed the effects of colored SJ resulting from the use of PLL-based oscillators to derive the sampling clocks for DACs and ADCs on the communication and sensing performance of OFDM-based ISAC for both BB and BP sampling strategies. After a mathematical formulation of the influence of SJ at the DAC and ADC at the transmitter and receiver sides, respectively, on an oversampled OFDM signal in Section II, communication and radar sensing performance analyses were presented.

The claim from [42] that DAC and ADC SJ have similar effects was also confirmed with the derived expression in (12), and the obtained results which showed that the combined RMS SJ, and not the individual DAC and ADC contributions, drive the performance of OFDM-based ISAC systems. Furthermore, simulation results indicated that the degradation

due to the considered colored SJ becomes noticeable when RMS SJ reaches approximately 10^{-11} s, which corresponds to 0.5×10^{-2} times the critical sampling period T_s , at both DAC and ADC for both BB and BP sampling. At this or higher SJ levels, non-negligible communication performance degradation is observed due to ICI in the BB sampling case and both ICI and CPE in the BP sampling case. Comparing this value with the 49.44 fs RMS SJ calculated based on the model for the Texas Instruments LMX2594 RF synthesizer [47] show in Fig. 1, it can be concluded that sufficient communication and radar sensing performance robustness against SJ can be achieved with state-of-the-art hardware.

While not covered by the analysis in this article, SJ may also bias the estimation and cause additional time and frequency synchronization offsets. This is, however, beyond the scope of this article and can be compensated, e.g., through synchronization offset estimation fine-tuning, as discussed and demonstrated in [33] within a bistatic OFDM-based ISAC context.

ACKNOWLEDGMENT

L. Giroto would like to thank Benedikt Geiger from the Karlsruhe Institute of Technology (KIT), Germany, for the valuable discussions, as well as Christian Maximilian Karle, also from KIT, for his support with the server PC used to conduct the simulations that produced the results presented in this article.

REFERENCES

- [1] M. Chafii, L. Bariah, S. Muhaidat, and M. Debbah, "Twelve scientific challenges for 6G: Rethinking the foundations of communications the-

- ory,” *IEEE Commun. Surv. Tut.*, vol. 25, no. 2, pp. 868–904, Second Quarter 2023.
- [2] C. de Lima et al., “Convergent communication, sensing and localization in 6G systems: An overview of technologies, opportunities and challenges,” *IEEE Access*, vol. 9, pp. 26 902–26 925, Jan. 2021.
 - [3] T. Wild, V. Braun, and H. Viswanathan, “Joint design of communication and sensing for beyond 5G and 6G systems,” *IEEE Access*, vol. 9, pp. 30 845–30 857, Feb. 2021.
 - [4] F. Liu et al., “Integrated sensing and communications: Towards dual-functional wireless networks for 6G and beyond,” *IEEE J. Sel. Areas Commun.*, vol. 40, no. 6, pp. 1728–1767, Jun. 2022.
 - [5] H. Wymeersch et al., “Joint communication and sensing for 6G - a cross-layer perspective,” in *2024 IEEE 4th Int. Symp. Joint Commun. Sens.*, Mar. 2024, pp. 01–06.
 - [6] A. Pärssinen et al., “White paper on RF enabling 6G: opportunities and challenges from technology to spectrum,” *University of Oulu*, 2021. [Online]. Available: <https://urn.fi/URN:ISBN:9789526228419>
 - [7] L. Giroto de Oliveira, B. Nuss, M. B. Alabd, A. Diewald, M. Pauli, and T. Zwick, “Joint radar-communication systems: Modulation schemes and system design,” *IEEE Trans. Microw. Theory Tech.*, vol. 70, no. 3, pp. 1521–1551, Mar. 2022.
 - [8] A. Kadelka, G. Zimmermann, J. Plachý, and O. Holschke, “A CSP’s view on opportunities and challenges of integrated communications and sensing,” in *2023 IEEE 3rd Int. Symp. Joint Commun. Sens.*, Mar. 2023, pp. 1–6.
 - [9] S. Mandelli, M. Henninger, M. Bauhofer, and T. Wild, “Survey on integrated sensing and communication performance modeling and use cases feasibility,” in *2023 2nd Int. Conf. 6G Netw.*, Oct. 2023, pp. 1–8.
 - [10] V. Shatov et al., “Joint radar and communications: Architectures, use cases, aspects of radio access, signal processing, and hardware,” *IEEE Access*, pp. 1–1, 2024.
 - [11] H. Viswanathan and P. E. Mogensen, “Communications in the 6G era,” *IEEE Access*, vol. 8, pp. 57 063–57 074, Mar. 2020.
 - [12] N. Rajatheva et al., “White paper on broadband connectivity in 6G,” *arXiv preprint arXiv:2004.14247 [eess.SP]*, Apr. 2020. [Online]. Available: <https://arxiv.org/abs/2004.14247>
 - [13] T. Hwang, C. Yang, G. Wu, S. Li, and G. Ye Li, “OFDM and its wireless applications: A survey,” *IEEE Trans. on Veh. Technol.*, vol. 58, no. 4, pp. 1673–1694, Aug. 2009.
 - [14] R. Thomä, T. Dallmann, S. Jovanoska, P. Knott, and A. Schmeink, “Joint communication and radar sensing: An overview,” in *2021 15th European Conf. Antennas Propag.*, Mar. 2021, pp. 1–5.
 - [15] T. Wild, A. Grudnitsky, S. Mandelli, M. Henninger, J. Guan, and F. Schaich, “6G integrated sensing and communication: From vision to realization,” in *2023 20th Eur. Radar Conf.*, Sept. 2023, pp. 355–358.
 - [16] C. B. Barneto et al., “Full-duplex OFDM radar with LTE and 5G NR waveforms: Challenges, solutions, and measurements,” *IEEE Trans. Microw. Theory Tech.*, vol. 67, no. 10, pp. 4042–4054, Oct. 2019.
 - [17] A. Nagulu et al., “Doubling down on wireless capacity: A review of integrated circuits, systems, and networks for full duplex,” *Proc. IEEE*, vol. 112, no. 5, pp. 405–432, May 2024.
 - [18] B. Smida, R. Wichman, K. E. Kolodziej, H. A. Suraweera, T. Riihonen, and A. Sabharwal, “In-band full-duplex: The physical layer,” *Proc. IEEE*, vol. 112, no. 5, pp. 433–462, May 2024.
 - [19] R. S. Thomä et al., “Cooperative passive coherent location: A promising 5G service to support road safety,” *IEEE Commun. Mag.*, vol. 57, no. 9, pp. 86–92, Sept. 2019.
 - [20] L. Smaini, *RF Analog Impairments Modeling for Communication Systems Simulation: Application to OFDM-based Transceivers*. New York, NY, USA: John Wiley & Sons, Ltd, 2012.
 - [21] V. D. Nguyen and H.-P. Kuchenbecker, “Intercarrier and intersymbol interference analysis of OFDM systems on time-invariant channels,” in *13th IEEE Int. Symp. Pers., Indoor Mobile Radio Commun.*, vol. 4, Sept. 2002, pp. 1482–1487.
 - [22] M. Speth, S. Fechtel, G. Fock, and H. Meyr, “Optimum receiver design for wireless broad-band systems using OFDM — Part I,” *IEEE Trans. Commun.*, vol. 47, no. 11, pp. 1668–1677, Nov. 1999.
 - [23] P.-Y. Tsai, H.-Y. Kang, and T.-D. Chiueh, “Joint weighted least-squares estimation of carrier-frequency offset and timing offset for OFDM systems over multipath fading channels,” *IEEE Trans. Veh. Technol.*, vol. 54, no. 1, pp. 211–223, Jan. 2005.
 - [24] Y. Wu, Y. Zhao, and D. Li, “Sampling frequency offset estimation for pilot-aided OFDM systems in mobile environment,” *Wireless Pers. Commun.*, vol. 62, pp. 215–226, Jan. 2012.
 - [25] A. Garcia Armada, “Understanding the effects of phase noise in orthogonal frequency division multiplexing (OFDM),” *IEEE Trans. Broadcast*, vol. 47, no. 2, pp. 153–159, Jun. 2001.
 - [26] V. Syrjala, M. Valkama, N. N. Tchamov, and J. Rinne, “Phase noise modelling and mitigation techniques in OFDM communications systems,” in *2009 Wireless Telecommun. Symp.*, Apr. 2009, pp. 1–7.
 - [27] K. Manoj and G. Thiagarajan, “The effect of sampling jitter in OFDM systems,” in *2003 IEEE Int. Conf. Commun.*, vol. 3, May 2003, pp. 2061–2065.
 - [28] V. Syrjala and M. Valkama, “Analysis and mitigation of phase noise and sampling jitter in OFDM radio receivers,” *Int. J. Microw. Wireless Technol.*, vol. 2, pp. 193–202, Apr. 2010.
 - [29] B. Nuss, J. Mayer, and T. Zwick, “Limitations of MIMO and multi-user access for OFDM radar in automotive applications,” in *2018 IEEE MTT-S Int. Conf. Microw. Intell. Mobility*, Apr. 2018, pp. 1–4.
 - [30] G. Hakobyan and B. Yang, “A novel intercarrier-interference free signal processing scheme for OFDM radar,” *IEEE Trans. Veh. Technol.*, vol. 67, no. 6, pp. 5158–5167, Jun. 2018.
 - [31] L. Wang, Z. Wei, L. Su, Z. Feng, H. Wu, and D. Xue, “Coherent compensation based ISAC signal processing for long-range sensing: (invited paper),” in *2023 21st Int. Symp. Model. Optim. Mobile, Ad Hoc, Wireless Netw.*, Aug. 2023, pp. 689–695.
 - [32] J. Pegoraro et al., “JUMP: Joint communication and sensing with unsynchronized transceivers made practical,” *IEEE Trans. Wireless Commun. (Early Access)*, pp. 1–16, Feb. 2024.
 - [33] D. Brunner et al., “Bistatic OFDM-based ISAC with over-the-air synchronization: System concept and performance analysis,” *arXiv preprint arXiv:2405.04962 [eess.SP]*, May 2024. [Online]. Available: <https://arxiv.org/abs/2405.04962>
 - [34] J. Aguilar, D. Werhun, V. Janoudi, C. Bonfert, and C. Waldschmidt, “Uncoupled digital radars creating a coherent sensor network,” *IEEE J. Microw.*, vol. 5, no. 3, pp. 459–472, Jun. 2024.
 - [35] L. Giroto de Oliveira et al., “Pilot-based SFO estimation for OFDM-based bistatic integrated sensing and communication,” *arXiv preprint arXiv:2407.07567 [eess.SP]*, Jul. 2024. [Online]. Available: <https://arxiv.org/abs/2407.07567>
 - [36] —, “On the sensing performance of OFDM-based ISAC under influence of oscillator phase noise,” *arXiv preprint arXiv:2410.13336 [eess.SP]*, Oct. 2024. [Online]. Available: <https://arxiv.org/abs/2410.13336>
 - [37] M. Löhning and G. Fettweis, “The effects of aperture jitter and clock jitter in wideband ADCs,” *Comput. Standards Interfaces*, vol. 29, pp. 11–18, Jan. 2007.
 - [38] B. D. Putra and G. Fettweis, “Clock jitter estimation and suppression in OFDM systems employing bandpass $\Sigma\Delta$ ADC,” in *2009 IEEE 10th Workshop Signal Process. Advances Wireless Commun.*, Jun. 2009, pp. 623–627.
 - [39] L. Yang and J. Armstrong, “Oversampling to reduce the effect of timing jitter on high speed OFDM systems,” *IEEE Commun. Lett.*, vol. 14, no. 3, pp. 196–198, Mar. 2010.
 - [40] U. Onunkwo, Y. Li, and A. Swami, “Effect of timing jitter on OFDM-based UWB systems,” *IEEE J. Sel. Areas Commun.*, vol. 24, no. 4, pp. 787–793, Apr. 2006.
 - [41] E. Haj Mirza Alian and P. Mitran, “Jitter-robust spectral shaping in OFDM,” *IEEE Trans. Commun.*, vol. 63, no. 4, pp. 1282–1290, 2015.
 - [42] O. F. A. Gonem, R. P. Giddings, and J. Tang, “Timing jitter analysis and mitigation in hybrid OFDM-DFMA PONs,” *IEEE Photon. J.*, vol. 13, no. 6, pp. 1–13, Dec. 2021.
 - [43] M. R. Khanzadi, D. Kuylentierna, A. Panahi, T. Eriksson, and H. Zirath, “Calculation of the performance of communication systems from measured oscillator phase noise,” *IEEE Trans. Circuits Syst. I, Reg. Papers*, vol. 61, no. 5, pp. 1553–1565, May 2014.
 - [44] B. Schweizer, D. Schindler, C. Knill, J. Hasch, and C. Waldschmidt, “On hardware implementations of stepped-carrier OFDM radars,” in *2018 IEEE/MTT-S Int. Microw. Symp.*, Jun. 2018, pp. 891–894.
 - [45] P. W. van der Walt and W. Steyn, “Characterizing phase noise in self-referencing radar,” *IEEE Aerosp. Electron. Syst. Mag.*, vol. 38, no. 12, pp. 4–13, Dec. 2023.
 - [46] Y. Li et al., “User detection in RIS-based mmWave JCAS: Concept and demonstration,” *IEEE Trans. Wireless Commun. (Early Access)*, pp. 1–16, Feb. 2024.
 - [47] Texas Instruments. *LMX2594 15-GHz Wideband PLLATINUM™ RF Synthesizer With Phase Synchronization and JESD204B Support* (2019). Accessed: Sept. 4, 2024. [Online]. Available: <https://www.ti.com/document-viewer/lmx2594/datasheet>.
 - [48] AMD. *Zynq UltraScale+ RFSoc RF Data Converter Evaluation Tool (ZCU111)* (2021). Accessed: Sept. 4, 2024. [Online]. Available: <https://docs.amd.com/v/u/en-US/ug1287-zcu111-rfsoc-eval-tool>.

- [49] Texas Instruments. *LMK04208 Low-Noise Clock Jitter Cleaner with Dual Loop PLLs* (2016). Accessed: Sept. 4, 2024. [Online]. Available: <https://www.ti.com/document-viewer/lmk04208/datasheet>.
- [50] C. Farrow, "A continuously variable digital delay element," in *1988 IEEE Int. Symp. Circuits Syst.*, vol. 3, Jun. 1988, pp. 2641–2645.
- [51] L. Erup, F. Gardner, and R. Harris, "Interpolation in digital modems — part II: Implementation and performance," *IEEE Trans. Commun.*, vol. 41, no. 6, pp. 998–1008, Jun. 1993.
- [52] G. Lellouch, A. K. Mishra, and M. Inggs, "Design of OFDM radar pulses using genetic algorithm based techniques," *IEEE Trans. Aerosp. Electron. Syst.*, vol. 52, no. 4, pp. 1953–1966, Aug. 2016.
- [53] Z. Liao et al., "Pulse shaping for random ISAC signals: The ambiguity function between symbols matters," *arXiv preprint arXiv:2407.15530 [eess.SP]*, Jul. 2024. [Online]. Available: <https://arxiv.org/abs/2407.15530>